

# High-contrast Computational Caustic Design

Yuli Schwartzburg

Romain Testuz

Andrea Tagliasacchi

Mark Pauly

EPFL



**Figure 1:** *Caustic Brain*: Our algorithm computes a 3D surface that refracts uniform light to focus on sharp intensity lines that sketch a human brain. The physical prototype shown on the right has been fabricated in transparent acrylic with a CNC milling machine. The photographs illustrate how the caustic image evolves as the acrylic piece is rotated into position (see also Figure 11 and accompanying video).

## Abstract

We present a new algorithm for computational caustic design. Our algorithm solves for the shape of a transparent object such that the refracted light paints a desired caustic image on a receiver screen. We introduce an optimal transport formulation to establish a correspondence between the input geometry and the unknown target shape. A subsequent 3D optimization based on an adaptive discretization scheme then finds the target surface from the correspondence map. Our approach supports *piecewise smooth* surfaces and non-bijective mappings, which eliminates a number of shortcomings of previous methods. This leads to a significantly richer space of caustic images, including smooth transitions, singularities of infinite light density, and completely black areas. We demonstrate the effectiveness of our approach with several simulated and fabricated examples.

**CR Categories:** I.3.5 [Computer Graphics]: Computational Geometry and Object Modeling—Physically based modeling;

**Keywords:** caustics, computational design, 3D optimization, inverse surface design

**Links:** [DL](#) [PDF](#) [WEB](#)

## 1 Introduction

The interplay of light and form is fundamental in how we perceive the world. Reflective or refractive objects exhibit particularly rich interactions with light, often creating fascinating caustic effects.

However, manually controlling the appearance of caustics is notoriously difficult, as slight changes to the specular surface can have large, non-local effects on the created caustic image. Objects such as the one shown in Figure 1 are virtually impossible to create with traditional means of shaping or sculpting a refractive material.

Instead, we follow a recent line of research that proposes computational solutions to approach this challenging inverse light transport problem [Finckh et al. 2010][Papas et al. 2011][Kiser et al. 2012][Yue et al. 2014]. We address fundamental shortcomings of these previous methods and propose the first solution capable of computing the shape of refractive objects that cast controlled, highly detailed caustic images of high contrast.

**Contributions.** We introduce a new optimization algorithm for inverse caustic design based on optimal transport. The optimal transport formulation in combination with an adaptive Voronoi discretization scheme enables a significantly broader range of target light distributions than previous methods. Our solution supports continuous, *piecewise smooth* surfaces to allow easy fabrication, while enabling

- high-contrast target images including completely black areas,
- point and curve singularities of infinite light density in the target image,
- non-uniform input light distributions with free boundaries on non-planar base geometries.

These features, that have not been shown in any previous method, significantly expand the creative possibilities of computational caustic design and enable caustic lighting for a variety of application domains, such interior and product design, lighting, architecture, or art. We present several prototypes that demonstrate that physical realizations of our caustic generators well match the predicted behavior.

**Related Work.** We briefly review several papers that are most closely related to our work. For a broader overview, we refer to the survey of Patow and Pueyo [2005] that provides an extensive discussion of methods for inverse surface design based on a desired light transport behavior. An interesting related survey focusing on

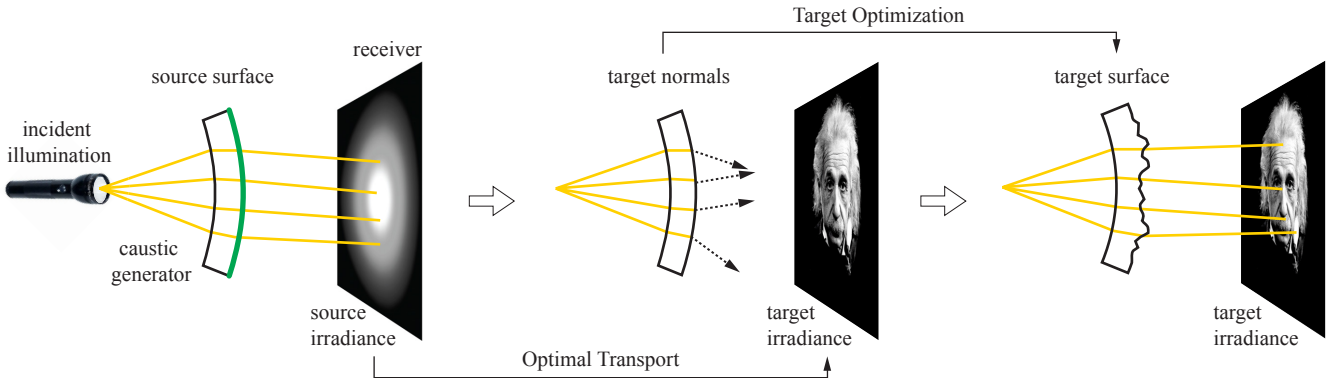


**Figure 2:** Processing pipeline. We first compute the initial source irradiance distribution on the receiver screen from the incident illumination. The optimal transport algorithm then finds a mapping to the target distribution from which we obtain the target normals on the source surface. The target optimization solves for the surface that best matches these normals. (Photo by Philippe Halsman © Philippe Halsman Archive)

computational tools to design and fabricate material appearance has been presented by Hullin et al. [2013]

One of the first methods in computer graphics to approach the caustic design problem is the work of Finck and colleagues [2010]. They use an analysis-by-synthesis strategy that stochastically perturbs a given input surface to better match the desired caustic image. While interesting results can be achieved with this approach, the optimization, even with an efficient GPU implementation, incurs a high computational cost and can be prone to local minima leading to undesirable artifacts in the generated image. Recently, there have been a number of papers related to our work that apply a more direct optimization approach. These can be divided into discrete patch-based approaches, and continuous parameterization-based methods.

Weyrich et al. [2009] generate a set of sloped, planar microfacets to realize a desired distribution of given ray directions. These microfacets are arranged in a regular grid using simulated annealing to minimize discontinuities. This approach is not designed to reproduce smooth distributions and does not scale well to high resolutions, which limits its applicability for caustic design. Papas et al. [2011] extend the microfacet approach to curved micropatches, which produce specks of light with an anisotropic Gaussian distribution. While significantly improving the quality of the caustic images, this method retains some of the discretization artifacts and has difficulties in resolving low intensity regions. This is mostly due to using a microfacet array rather than a continuous surface. Nevertheless, there are similarities between our approach. They model the target image distribution as discrete Gaussian kernels and use capacity-constrained Voronoi tessellations for discretization. We model the target exactly and use Lloyd iterations to initialize a power diagram as discretization. While their approach uses simulated annealing to find a mapping, we use optimal transport.

Yue et al. [2012] propose a different optimization approach using reconfigurable prismatic sticks that refract parallel light onto a screen. Their focus is on creative applications where several discrete images can be generated with a single set of refractive sticks. Beyond the limited resolution and other visual deficiencies, a main difficulty with these discrete approaches is that they need to solve a complex spatial arrangement problem. These typically leads to a NP-hard optimizations that require approximation solvers.

Yue et al. [2014] and Kiser et al. [2012] address this problem by formulating a continuous optimization. Their solutions can produce smooth surfaces that lead to a significant improvement in the quality of the caustic images. The core idea is to find a continuous bijective

mapping between incoming light and caustic image through a 2D parameterization that locally adapts area to match the desired target brightness. However, enforcing smoothness globally and requiring a one-to-one mapping is unnecessarily restrictive and thus limits the type of caustic images that can be produced. High-contrast regions, intense concentrations of light, or completely black areas are very difficult to achieve this way, as they lead to large deformations of the underlying geometry (see Figure 3). In contrast, our algorithm alleviates these difficulties by automatically introducing discontinuities in the normal field at optimally chosen locations. In addition, our mapping is not constrained to be bijective, enabling intense concentrations of light onto singular points or curves.

Our work is also related to research in computational optics. Glimm and Oliker [2003] investigated inverse reflector design for far-field distributions, where only the direction of a reflected ray is considered. They showed that certain far-field reflectors can be modeled by a 2nd order nonlinear elliptic PDE of Monge-Ampere type, which can be solved in variational form using Monge-Kantorovich mass transfer. This work, while using very different assumptions and constraints than our solution, inspired our use of an optimal transport formulation.

Numerous other works investigate the design and fabrication of freeform optical systems with applications in energy, lasers, illumination, or biomedical imaging, for example. A detailed discussion of this body of work is beyond the scope of this paper, we refer instead to [Fang et al. 2013] for a survey of recent developments. In general, the objectives of these methods are substantially different from ours, ranging from aberration correction, reflector or lens design for light sources such as LEDs, to solar concentration. In contrast, our work aims at precise control of visually complex caustic projection images with a focus on applications in design, art, and architecture.

## 2 Overview

We first introduce some terminology and give a high-level overview of our approach as illustrated in Figure 2. We assume we are given the initial geometry refractive object, the *caustic generator*, and the incident illumination on that object. The user also specifies the position and orientation of a *receiver* screen on which the desired caustic image should appear. The receiver is typically a diffuse planar surface of arbitrary orientation. The incident illumination is refracted through the initial geometry to create an irradiance distribution on the receiver that we call the *source irradiance*  $E_s$ . Our goal is to determine the shape of the caustic generator such that

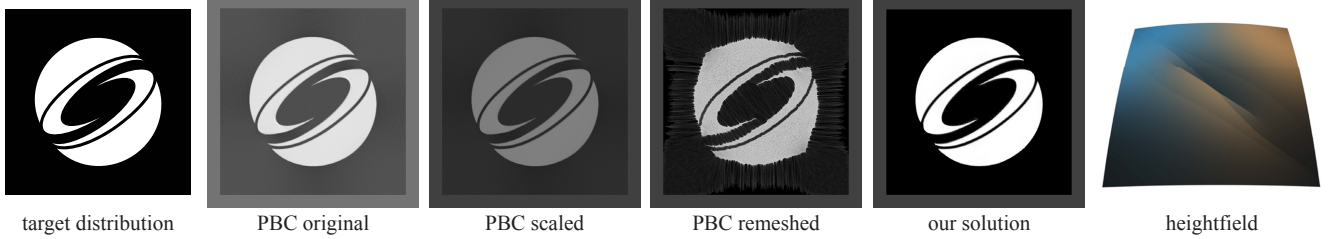


**Figure 3:** Comparison of our method to the Poisson-based continuous (PBC) method of [Yue et al. 2014]. Their algorithm needs to artificially reduce contrast to match the shape of the logo. The original image is taken from the paper. The scaled image matches the overall light intensity of our solution, as indicated by the gray border that shows the intensity of the uniform input illumination. An extension of PBC that dynamically remeshes the domain yields strong distortion artifacts. In contrast, our result achieves high caustic image quality. All PBC results have been produced by the authors of [Yue et al. 2014].

the resulting irradiance distribution on the receiver matches a desired *target irradiance*  $E_T$  provided by the user.

To formulate our optimization we make several simplifying assumptions. We use a geometric model of optics with perfect specular scattering. To create the desired caustic image, we only modify a single scattering event for each light path, i.e. we change the shape of a single refractive surface that we call the *source surface*. The optimized surface computed by our algorithm is the *target surface*. Light rays should arrive at each point of the source surface from a single direction only, which requires idealized illumination such as parallel light or light emitted by point sources. We comment on the effect of area light sources in Section 6.

Our algorithm first calculates the source irradiance  $E_S$  by raytracing the incident illumination through the source geometry. Then we compute an optimal transport map (OTM) from source to target on the receiver screen. This map encodes how the distribution of light needs to be modified to obtain the desired target image. More specifically, we compute a target position on the receiver for each light ray that leaves the source surface. Using Snell’s law we can then determine appropriate normals on the source surface that can be integrated to obtain the optimized target surface.

We first describe how to define the target distribution in Section 3. The subsequent sections discuss the core components of our algorithm: Section 4 explains how to compute an OTM using an optimization on a power diagram, while Section 5 describes an iterative optimization algorithm to compute the 3D surface of the caustic generator from the OTM. In Section 6 we present several simulated and physical results and provide an evaluation and comparison of our method with previous work. We conclude with remarks on future research direction in Section 7.

### 3 Specifying the Target

As described in detail below, we use an optimal transport formulation to map the source irradiance  $E_S$  to the target  $E_T$  in order to compute the target positions on the receiver for each refracted light ray. In this setup, source and target are more conveniently represented as *radiant flux measures*  $\Phi_S$  and  $\Phi_T$ , respectively. A measure is a function that assigns a non-negative real number to subsets of a domain, satisfying certain properties such as non-negativity and countable additivity [Bogachev 2006]. We make use of this representation in Section 4.

Flux  $\Phi$  and irradiance  $E$  are related as  $\Phi(\Omega) = \int_{\Omega} E(x, y) dx dy$  for any subset  $\Omega \subseteq \mathbb{R}^2$ . Let  $U$  be the union of the supports of  $\Phi_S$  and  $\Phi_T$  on the receiver, i.e. the smallest closed set such that  $\Phi_S(\mathbb{R}^2 \setminus U) = \Phi_T(\mathbb{R}^2 \setminus U) = 0$ . In the following, we drop the

subscript for a radiant flux that can refer to either  $\Phi_S$  and  $\Phi_T$ .

**Singularities.** One of the most fascinating features of caustics is the intense concentration of brightness when light is sharply focused onto points or curves. To capture this effect we support point and curve singularities of infinite light density in our target distribution  $\Phi_T$ . These can be represented using point and line Dirac delta distributions [Zhang and Zheng 2012]. We define three types of base functions  $\Phi_0$ ,  $\Phi_1$ , and  $\Phi_2$  for point singularities, curve singularities, and area distributions, respectively. We specify point and curve singularities through an SVG file and area distributions as either an SVG file or a PNG image. These base functions can then be combined arbitrarily to build the desired target distribution  $\Phi_T$ .

A point singularity  $\delta$  is specified by a position  $\mathbf{x}_\delta \in U$  and a flux  $\Phi_\delta$ , such that

$$\Phi_0(\Omega) = \begin{cases} \Phi_\delta & \text{if } \mathbf{x}_\delta \in \Omega \\ 0 & \text{otherwise.} \end{cases}$$

A curve singularity  $\gamma$  is represented by a curve  $c : [0, L] \rightarrow \mathbb{R}^2$  and a curve density function  $f : [0, L] \rightarrow \mathbb{R}$ , where  $c$  is parameterized with respect to arc length and  $L$  is the total length of  $c$ . Then  $\Phi_1$  is defined as

$$\Phi_1(\Omega) = \int_0^L f_\Omega(t) dt,$$

where is  $f_\Omega$  the restriction of  $f$  onto  $\Omega$ :

$$f_\Omega = \begin{cases} f(t) & \text{if } c(t) \in \Omega \\ 0 & \text{otherwise.} \end{cases}$$

Finally, we define

$$\Phi_2(\Omega) = \int_{\Omega} E(x, y) dx dy,$$

where  $E : U \rightarrow \mathbb{R}$  is an integrable 2D irradiance function.

**Target.** Let  $\{\delta_1, \dots, \delta_{N_\delta}\}$  be a set of  $N_\delta$  point singularities and  $\{\gamma_1, \dots, \gamma_{N_\gamma}\}$  a set of  $N_\gamma$  curve singularities. The target flux function  $\Phi_T$  is then represented by the combination of 0, 1, and 2-dimensional integral functions as

$$\Phi_T(\Omega) = \sum_{i=1}^{N_\delta} \Phi_0^i(\Omega) + \sum_{j=1}^{N_\gamma} \Phi_1^j(\Omega) + \Phi_2(\Omega). \quad (1)$$

We model curve singularities with piecewise linear representations. Unlike previous work, these singularities allow infinite light density.

To represent the 2D irradiance function  $E$  we support a pixel grid of intensity values or a vector representation. Note that both the source and the target distributions can contain regions of zero intensity anywhere in  $U$ . In particular for the target, completely black regions are not possible in previous methods that use continuous generator surfaces.

## 4 Optimal Transport

The goal of computational caustic design is to redirect light rays such that the desired target light image is drawn on the receiver screen. Since we assume a mostly diffuse receiver that scatters light equally in all directions, the perception of the caustic image depends mainly on the flux density or irradiance at each point, but is largely independent of the direction of the incoming rays hitting the screen. This means that we can formulate the optimization on the target positions of each light ray on the receiver. In other words, we need to answer the question: How do we have to move the initial source positions of each ray on the receiver towards new target positions, such that the overall irradiance distribution matches the target  $E_T$  as closely as possible? We solve this problem using an optimal transport formulation to compute the target positions. As we discuss below, optimal transport is ideally suited to handle discontinuities and singularities, while maximizing smoothness to obtain high caustic image quality.

### 4.1 Continuous Optimal Transport

We briefly review the basic concepts of optimal transport that are most relevant for our approach. For an extensive review we refer to [Villani 2009]. Optimal transport is concerned with finding a mapping between two probability measures, a source measure  $\mu_S$  and a target measure  $\mu_T$ . A 2D *transport map* from  $\mu_S$  to  $\mu_T$  is a function  $\pi : U \rightarrow U$  for some domain  $U \subseteq \mathbb{R}^2$ , such that  $\mu_S(\Omega) = \mu_T(\pi(\Omega))$  for every subset  $\Omega \subseteq U$ . We can define a global transport cost for  $\pi$  as

$$c(\pi) = \int_U \|x - \pi(x)\|^2 d\mu_S(x).$$

For this  $\ell_2$  cost measure it has been shown that there exists a unique *optimal transport map* (OTM) that is a global minimizer of the total transport cost [Villani 2009]. Minimizing the transport cost in our context means that overall the directions of the refracted light rays are modified as little as possible. This minimizes the change in curvature of the target surface and ensures that no foldovers are introduced in the mapping. Among other benefits (see discussion below), this simplifies physical fabrication and helps avoid optical deficiencies such as internal reflections.

To apply the optimal transport formalism to our problem, we need to transform our radiant flux measures  $\Phi_S$  and  $\Phi_T$  into probability measures, i.e. measures of total mass of one. This can be easily achieved as

$$\mu_S(\Omega) := \frac{\Phi_S(\Omega)}{\Phi_S(U)}, \quad \mu_T(\Omega) := \frac{\Phi_T(\Omega)}{\Phi_T(U)}, \quad (2)$$

where  $\Phi_S(U) = \Phi_T(U)$  is the total mass of  $\Phi$ , assuming that no light is lost due to absorption.

### 4.2 Discrete Optimal Transport

Our computation of the discrete OTM follows the algorithm introduced by Aurenhammer et al. [1998] and later extended and improved by Merigot [2011]. A similar approach has been proposed by de Goes et al. [2012].

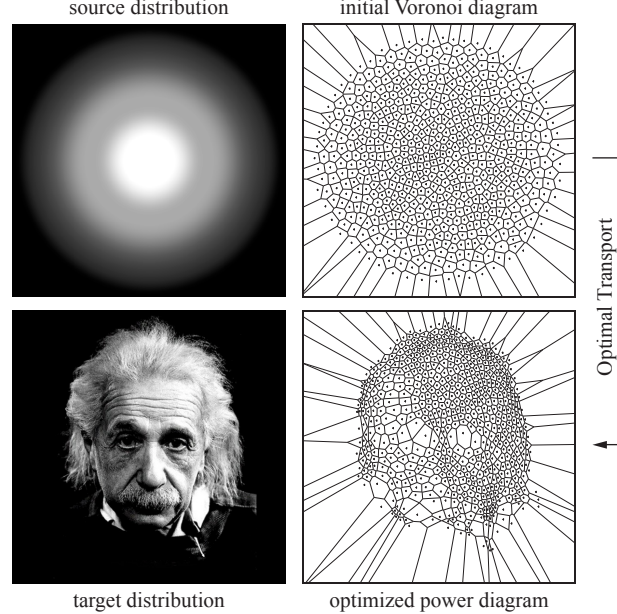


**Figure 4:** The source irradiance distribution is sampled using Lloyd sampling to obtain the initial Voronoi diagram, where each Voronoi cell approximately receives the same irradiance (low resolution for illustration). The optimization then computes the weights of the corresponding power diagram that best matches the target distribution. The dots show the centers of mass of the source and target distribution, respectively, integrated over the cells. (Photo by Philippe Halsman © Philippe Halsman Archive)

We assume that the incident illumination is represented as a triangle mesh on the source surface, where each vertex carries an incoming direction and an intensity value. This triangle mesh is ray-traced through the source surface onto the receiver screen to obtain a piecewise linear representation of the source irradiance  $E_S$ . Here we assume that the refraction through the source surface does not create any fold-overs or singularities.

We resample  $E_S$  such that each sample roughly represents the same amount of flux to best exploit the degrees of freedom in the OTM optimization. For this purpose, we apply Lloyd sampling on  $E_S$  to obtain a set  $\mathcal{S} = \{\mathbf{s}_1, \dots, \mathbf{s}_n\}$  of sites  $\mathbf{s}_i \in U$ . The domain  $U$  is then discretized using a Voronoi diagram of  $\mathcal{S}$ . The goal is to determine how each Voronoi cells need to be deformed and moved, such that its flux is distributed to match the desired target distribution. This can be achieved by representing the target distribution as a power diagram (weighted Voronoi diagram) on the sites  $S$  and finding suitable weights (see Figure 4).

Let  $P_\omega$  be the power diagram of  $\mathcal{S}$  with a set of weights  $\omega = \{\omega_1, \dots, \omega_n\}$ . When all weights  $\omega_i$  are zero, the power diagram coincides with the Voronoi diagram, which we thus denote as  $P_0$ . Let  $C_i^\omega$  be the power cell of  $P_\omega$  associated with site  $\mathbf{s}_i$ . Aurenhammer and colleagues [1998] have shown that there is a unique assignment of weights such that  $\mu_S(C_i^0) = \mu_T(C_i^\omega)$  for all  $i$ .

Recalling the definitions of Equations 1 and 2, this means that for a suitable set of weights  $\omega$ , light refracted by the initial base geometry onto the Voronoi cell  $C_i^0$  on the receiver will be redirected to the power cell  $C_i^\omega$  of  $P_\omega$ . The ratio of areas of  $C_i^0$  and  $C_i^\omega$  accounts for the relative difference of intensity in the source and target.

Merigot [2011] showed that the unknown weight vector  $\omega$  can be

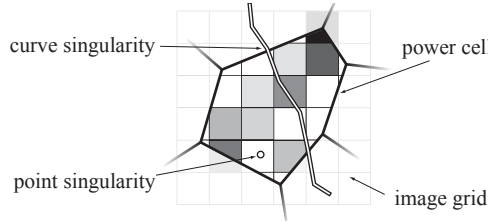


**Figure 5:** Integration of the target measure on a power cell. Curve singularities are approximated by piecewise linear segments.

found as a global minimizer of the convex function

$$f(\omega) = \sum_{s_i \in S} \left( \omega_i \mu_S(C_i^0) - \int_{C_i^\omega} (\|\mathbf{x} - \mathbf{s}_i\|^2 - \omega_i) d\mu_T(\mathbf{x}) \right). \quad (3)$$

This result is fundamental for our algorithm as it ensures that the OTM can be found by a suitable gradient descent scheme. It turns out that the corresponding gradients are simply the differences of the integrated source and target densities, i.e.

$$\frac{\partial f}{\partial \omega_i} = \mu_S(C_i^0) - \mu_T(C_i^\omega). \quad (4)$$

We use an L-BFGS solver [Liu and Nocedal 1989] to minimize the objective function  $f$  of Equation 3, following the multi-scale strategy proposed in [Mérigot 2011]. We refer to this paper for detailed derivations and implementation details. In all our examples the number of points is scaled by a factor of four between two different levels of the multi-scale solver. We use the CGAL library [Yvinec 2013] with exact arithmetic to compute the power diagrams.

**Singularities.** Mérigot’s solution maps a source density to a finite set of point sites. We use an inverse formulation, i.e. we map a set of sites, the samples on the source distribution, to the density defined by the target measure. This allows us to naturally integrate singularities in the target measure by adapting the calculations of the integrals in Equations 3 and 4 (see Figure 5). We split the integrals over the target measure on each power cell into separate terms according to Equation 1 and evaluate each term separately. Point singularities are trivial to evaluate. For curve singularities, we approximate each curve by a polygon segment and the corresponding density by a piecewise linear function defined over the polygon, leading to a simple analytical formula for the integration (see Section 3). To

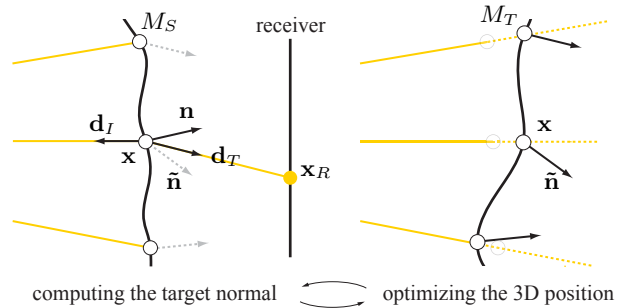


**Figure 6:** Two-stage target optimization. We first compute the target normal  $\hat{\mathbf{n}}$  for each vertex (left), then solve for the vertex position  $\mathbf{x}$  to obtain the target surface that matches these normals (right). Because  $\mathbf{x}$  changes, the target direction  $\mathbf{d}_T$  and consequently the normal  $\hat{\mathbf{n}}$  need to be updated, hence both stages are iterated.

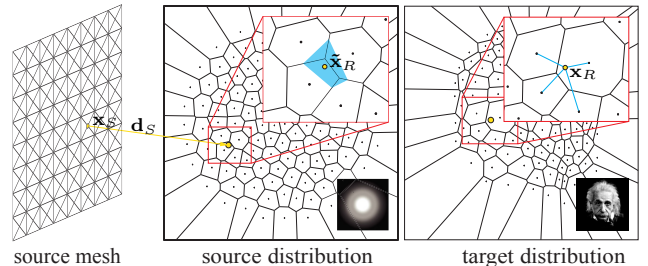


**Figure 7:** Natural neighbor interpolation of the OTM onto the vertices of the source mesh. First we obtain  $\tilde{\mathbf{x}}_R$  as the intersection with the receiver plane of the ray leaving the source surface at  $\mathbf{x}_S$  in direction  $\mathbf{d}_S$ . Inserting this point into the Voronoi diagram of the source distribution yields the blue cell. The fraction of area of each original Voronoi cell that the blue cell covers defines the interpolation weights for computing the target position  $\mathbf{x}_R$  from the corresponding centroids of the target power diagram (right).

evaluate integrals over pixel areas and similarly for filled polygons, we first compute the intersection of each pixel with the cell to adapt the pixel boundaries appropriately. We assume constant density for each pixel area and apply Green’s theorem to transform the area integral into a simpler boundary integral. A benefit of our optimal transport formulation compared to previous methods [Kiser et al. 2012; Yue et al. 2014] is that the OTM is not required to be bijective. This means, for example, that we can focus light going through a certain area of the generator onto a single point or curve, thus creating singularities of infinite light density.

**Discontinuities.** The regularity of optimal transport has been studied extensively, see [De Philippis and Figalli 2013] for a recent survey. Essentially, OTMs are continuous for a quadratic cost function like the one we use, if the probability measures are sufficiently regular and the target convex. Nevertheless, discontinuities arise naturally in optimal transport for non-convex or high-contrast targets, see [Chodosh et al. 2013] for a sufficient condition for discontinuity in planar OTMs. Adjacent regions in the source can be mapped to distant regions on the target, which leads to discontinuities in the normals of the target surface. These discontinuities are in fact necessary when aiming at completely black interior regions, for example (see Figure 9). This additional flexibility to introduce discontinuities in the mapping is a major benefit of optimal transport, as it strongly reduces distortion artifacts commonly observed in globally smooth methods such as [Kiser et al. 2012; Yue et al. 2014] (see also Figures 12 and 3).

## 5 Target Optimization

The OTM provides us with a discrete mapping between source and target irradiance distributions. More precisely, it provides the positions where rays leaving the source surface *should* intersect the receiver. The goal of the target optimization is now to find the corresponding target surface that refracts the rays towards these target positions. For this purpose we discretize the target surface with a triangle mesh that is initialized on the source surface. We compute target normals for each vertex, using Snell’s law, from the target ray directions derived from the OTM. The optimization then moves the vertices to best match these normals while respecting the desired flux densities. Since modifying the vertex positions changes the target directions, we iterate this process (see Figure 6).

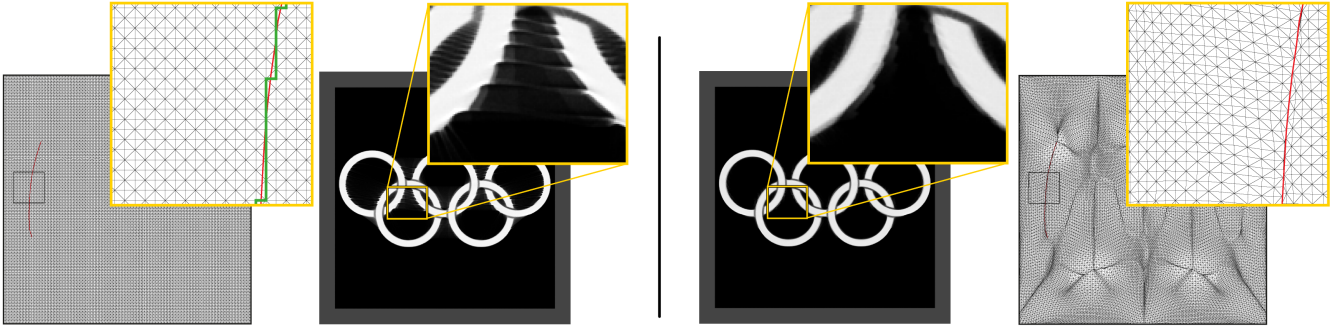


**Figure 8:** Benefit of 3D integration. Left: The result of our optimal transport algorithm integrated on a regular height field, as used in previous integration methods [Kiser et al. 2012; Yue et al. 2014]. Since the grid cannot align with the sharp creases produced by discontinuities in the OTM, artifacts appear at high contrast transitions. Right: Our full 3D integration scheme largely avoids these artifacts by properly aligning mesh edges to the creases. (SVG source: Wikipedia. The Olympic Rings are ® International Olympic Committee)

**OTM Interpolation.** As illustrated in Figure 4, the power diagram adapts to the target distribution and can thus be highly non-uniform. However, for light transport simulation or fabrication, a uniform sampling of the target surface is preferable. We therefore represent the target surface by a uniform triangle mesh  $M_T$  of user-specified resolution. Let  $v = \{\mathbf{x}, \mathbf{n}, \mathbf{d}_I, \mathbf{x}_R\}$  be a vertex of  $M_T$ , where  $\mathbf{x}$  is the vertex position,  $\mathbf{n}$  the corresponding surface normal,  $\mathbf{d}_I$  the direction of the incoming ray, and  $\mathbf{x}_R$  the intersection of the outgoing ray with the receiver; see Figure 6. The positions  $\mathbf{x}$  and incoming ray directions  $\mathbf{d}_I$  are initialized from the source surface and incoming illumination, respectively. We retrieve the target position  $\mathbf{x}_R$  from the OTM. Recall that the OTM defines a point-wise correspondence between the weighted centroid of each Voronoi cell and the corresponding power cell. To obtain the target position  $\mathbf{x}_R$  we interpolate the computed receiver positions onto  $M_S$  using natural neighbor interpolation [Sibson 1981], as shown in Figure 7. Since natural neighbor interpolation is only defined within the convex hull of the centroids, we extrapolate by moving the centroids of boundary cells onto the boundary. This causes a slight deformation at the boundary, but the effect diminishes as the OTM resolution increases.

Given an incoming light vector  $\mathbf{d}_I$  and a target direction  $\mathbf{d}_T = (\mathbf{x}_R - \mathbf{x}) / \|(\mathbf{x}_R - \mathbf{x})\|$ , we compute the desired target surface normal using Snell’s law as  $\tilde{\mathbf{n}} = \mathbf{d}_I + \eta \mathbf{x} / \|\mathbf{d}_I + \eta \mathbf{d}_T\|$ , where  $\eta$  is the ratio of the refraction indices of the two media. We refer to [Kiser and Pauly 2012] for a derivation of this formula.

**3D Optimization.** Even though the OTM is curl-free, the normals derived from the corresponding targets are not necessarily integrable, due to the non-linearity introduced by Snell’s law. To compute the target surface, we thus formulate an iterative optimization that solves for the target vertex positions by minimizing the following compound energy:

$$\arg \min_{\mathbf{x}} \mathbf{w} \cdot [E_{\text{int}}, E_{\text{dir}}, E_{\text{flux}}, E_{\text{reg}}, E_{\text{bar}}], \quad (5)$$

where  $\mathbf{w}$  is a weighting vector. The integration energy aligns the vertex normals  $\mathbf{n}$  of  $M_T$  with the target normals  $\tilde{\mathbf{n}}$  derived from the OTM:

$$E_{\text{int}} = \sum_{v \in M_T} \|\mathbf{n} - \tilde{\mathbf{n}}\|_2^2, \quad (6)$$

where  $\mathbf{n}$  is computed by averaging the normals of incident triangles weighted by the incident angles [Botsch et al. 2010, Pg.41]. Previous techniques constrain the vertices of  $M_T$  to lie on the associated incoming ray direction and therefore only need to solve for a scalar vertex displacement. As illustrated in Figure 8, this can be problematic, because the mesh cannot adapt to sharp creases caused by

discontinuities in the normal field. We therefore perform the optimization over all spatial coordinates of the mesh to allow vertices to slide along the surface to better represent crease lines. However, to maintain consistency with the OTM, we need to ensure that vertices do not deviate too much from the incoming ray direction. This can be achieved with a penalty term

$$E_{\text{dir}} = \sum_{v \in M_T} \|\mathbf{x} - \mathbf{proj}_{(\mathbf{x}_S, \mathbf{d}_I)}(\mathbf{x})\|_2^2, \quad (7)$$

where  $\mathbf{x}_S$  is the position of vertex  $v$  on the source surface. The projection operator  $\mathbf{proj}$  returns the point on the line  $(\mathbf{x}_S, \mathbf{d}_I)$  closest to  $\mathbf{x}$ . In addition, we need to ensure that the flux over triangle  $t$  of  $M_T$  remains constant, because the OTM was computed according to this flux. Therefore, we insert a flux preservation energy for each triangle:

$$E_{\text{flux}} = \sum_{t \in M_T} \|\Phi_T(t) - \Phi_S(t_S)\|^2, \quad (8)$$

where  $t_S$  is the triangle corresponding to  $t$  on the source surface. To maintain well-shaped triangles we add the regularization term:

$$E_{\text{reg}} = \|\mathbf{LX}\|_2^2, \quad (9)$$

where the vertices of  $M_T$  are stacked in  $\mathbf{X}$ , and  $\mathbf{L}$  is the corresponding combinatorial Laplacian matrix [Botsch et al. 2010]. Finally, we introduce an additional barrier energy to ensure the physical realizability of the piece by preventing the surface to fall beyond a certain distance  $d_{TH}$  from the receiver:

$$E_{\text{bar}} = \sum_{v \in M_T} \|f_{\text{bar}}(\mathbf{n}_R \cdot (\mathbf{x} - \mathbf{x}_R))\|^2 \quad (10)$$

$$f_{\text{bar}}(x) = \max(0, -\log((1 - x) + d_{TH})) \quad (11)$$

where  $\mathbf{n}_R$  is the normal of the receiver plane.

The pseudocode of the target optimization algorithm is provided below.

We solve Equation 5 using the auto-differentiation Levenberg-Marquadt optimization offered by the *Ceres* framework [Agarwal et al. 2013]. The optimization converges after a few outer iterations of Fresnel Mapping followed by 3D optimization.

For all our examples, we set the weights for  $E_{\text{int}}$  and  $E_{\text{bar}}$  to 1. For the Einstein, Olympic, and Brain models we use  $1 \times 10^{-6}$  for the weight of  $E_{\text{dir}}$  and no flux energy, while the Siggraph and Lena models are computed with  $1 \times 10^{-4}$  for  $E_{\text{dir}}$  and  $1 \times 10^{-3}$  for  $E_{\text{flux}}$ . The

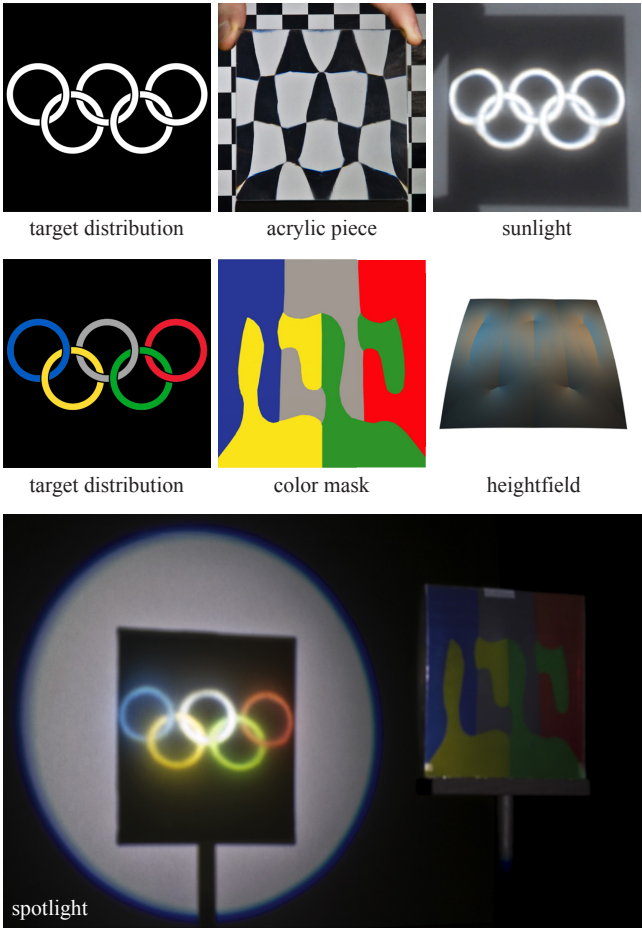


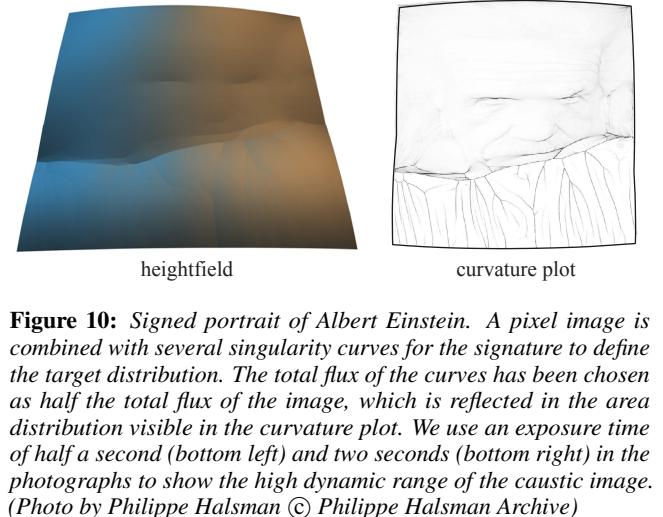
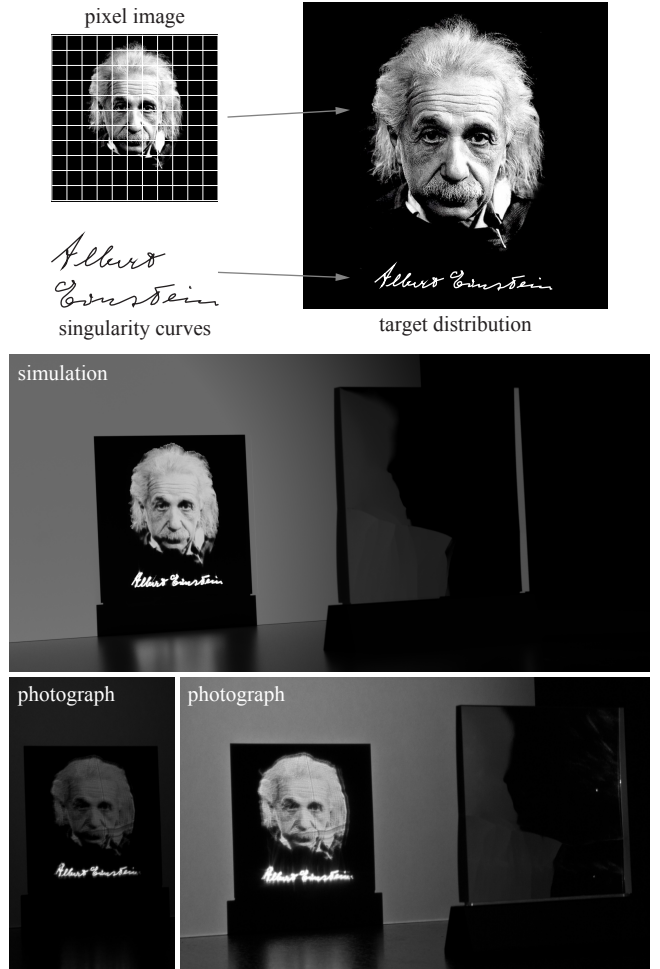
**Figure 9:** A caustic image of the Olympic rings photographed under sunlight (top right) and a spotlight (bottom) with a color mask computed from the OTM.

```

// INPUT:
//   X := vertex positions of M_S
//   R := optimal transport map
// OUTPUT:
//   X := vertex positions of M_T
function X = TARGET-OPTIMIZATION(X, R)
  X_R = OTM-Interpolation(X, R)
  while NotConverged() do
    D_T = normalize(X_R - X)
    N = Fresnel-Mapping(X, D_T)
    X = Normal-Integration(X, N)
  end while
end function

```

results are not particularly sensitive to the choice of these parameters. More difficult to tune is the weight for regularization term  $E_{\text{ref}}$  (we select values between  $1 \times 10^{-6}$  and  $1 \times 10^{-4}$  in our examples). If chosen too low, triangle inversions might occur that lead to an inconsistent surface. On the other hand, if the weight is too high, we deviate from the optimal solution, which introduces distortions in the caustic image. In the future we want to investigate more sophisticated regularization terms that prevent triangle inversions without negatively affecting the other objectives.



## 6 Results and Discussion

In this section we present several simulated results and physical prototypes computed by our optimization algorithm. We also evaluate the approximation quality with a ground truth example, compare our solution to previous methods, and comment on limitations of our approach. Please also refer to the accompanying video for dynamic

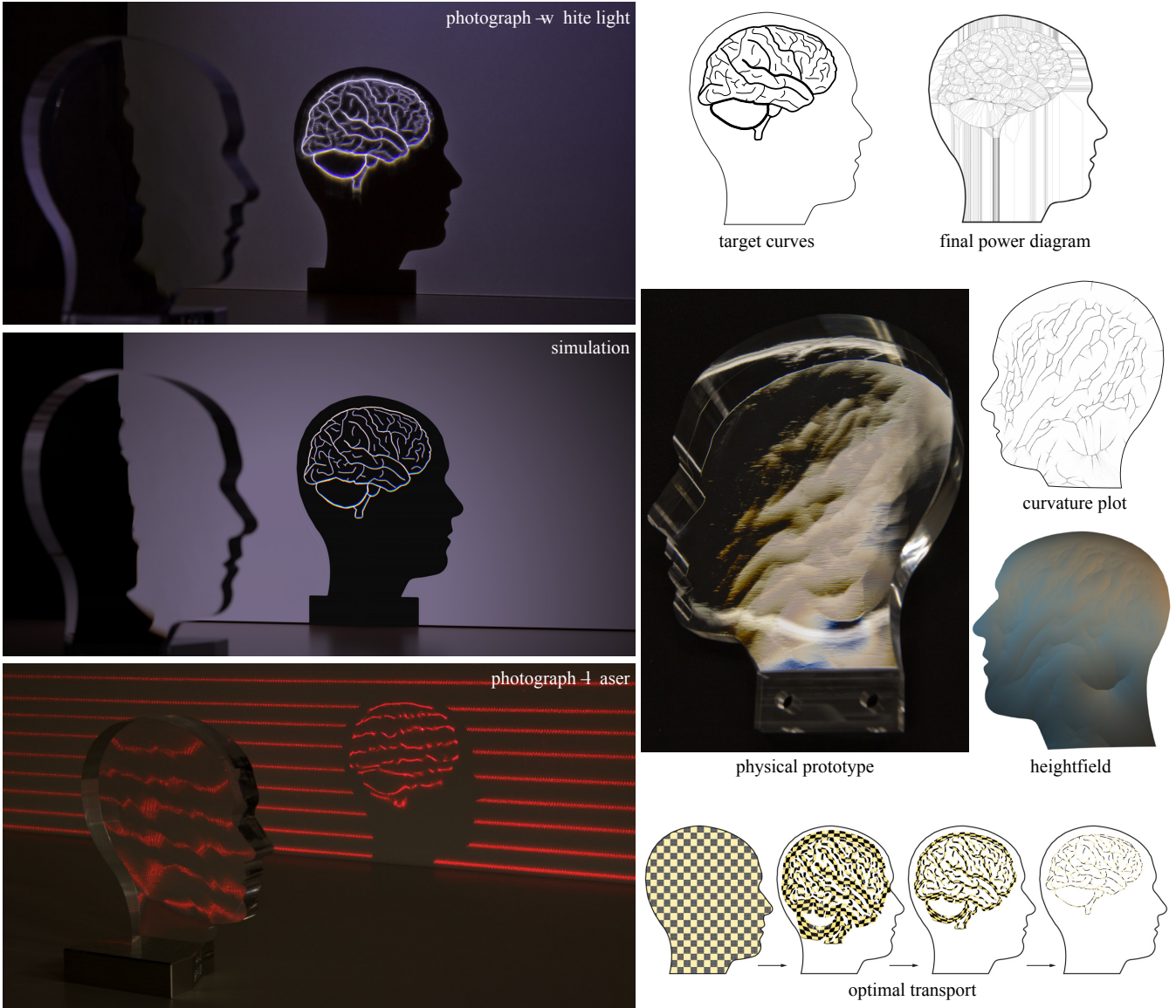


**Figure 11:** The caustic generator of the brain. The target distribution is composed of a number of singularity curves, where the line thickness indicates the relative flux density of each line. Computed from an initial uniform sampling, the final power diagram (1/4 the sample size for better readability) illustrates the highly non-uniform discretization necessary to match the target. The bottom-right row shows how a set of regularly sampled points is transported under the OTM. At left, a comparison of the physical prototype with a light transport simulation computed with LuxRender with roughly the same camera and light source parameters, and a photograph of horizontal laser beams demonstrating how light is refracted.

results. All light transport simulations have been generated using the physics-based rendering software *LuxRender*.

Figures 1 and 11 show a challenging example on a freeform domain. The high concentration of uniform light onto a complex network of singular curves of varying intensity and separated by black regions, is achieved through numerous discontinuities in the OTM. Figure 9 shows another high contrast caustic with completely black interior and exterior regions. The distortion of the checkerboard illustrates the strong refraction of the caustic generator. A simple extension allows for colored caustics. If the target distribution is wavelength-dependent, e.g. given by a color image, we can create a corresponding semi-transparent color filter on the caustic generator based on the OTM. The resulting color mask nicely illustrates how the incoming illumination is distributed towards the different rings.

Note how no light is lost to the background in these examples (see also Figure 12). This kind of effect can only be achieved by adequate handling of discontinuities. Figure 10 combines a smooth image with high-intensity singularity lines. Although there are slight distortions due to fabrication errors, the result retains its high contrast and quality.

The setup for each example is listed as follows:

Image	Mesh size	OT samples	Physical size	$d_{TH}$
EINSTEIN	$641^2$	261k	$10 \text{ cm}^2$	30 cm
OLYMPIC	$641^2$	261k	$10 \text{ cm}^2$	30 cm
BRAIN	$641^2$	163k	$11.5 \times 13.5 \text{ cm}$	40 cm
SIGGRAPH	$641^2$	254k	$10 \text{ cm}^2$	30 cm
LENA	$1281^2$	1.3m	$10 \text{ cm}^2$	10 cm

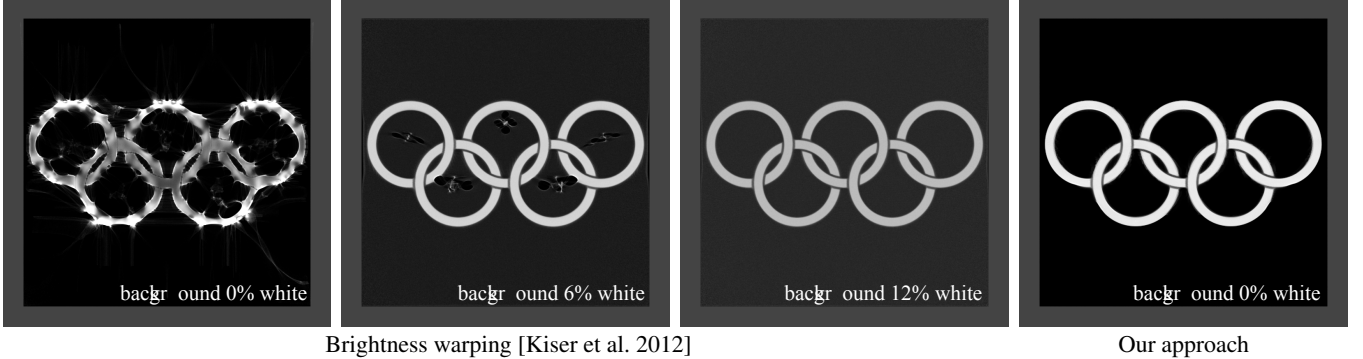


**Figure 12:** Comparison of our approach to the approach of [Kiser et al. 2012]. This method exhibits strong distortions for a black background (left). These artifacts can be reduced by brightening the background at the cost of reduced contrast. The artifacts disappear completely at about 12% white background, but now only 50% of the total incident illumination is focused on the rings. The gray border indicates the intensity of the uniform input illumination. All brightness warping results have been generated by the authors of [Kiser et al. 2012].

**Fabrication.** The physical prototypes are fabricated in acrylic (PMMA, IOR: 1.49) using the Mikron HSM 400U 5-axis CNC milling machine. Milling is performed in three passes: one with a 10 mm diameter standard drafting mill, and two with a 4 mm diameter diamond drill. The final pass is done with a cusp height of 1.5 microns at 36,000 RPM. After milling, the necessary polishing is done by hand with a PMMA polish paste. We refer to [Pauly et al. 2013] for more details and experiments related to the fabrication process.

**Performance.** Thanks to the multi-scale approach of the OTM optimization, we empirically observe roughly linear complexity in the number of input samples. However, each iteration requires re-computing the power diagram using exact arithmetic, which is computationally involved. For the example in Figure 9, it took 4 minutes for 16 thousand points, 25 minutes for 66 thousand points, and 95 minutes for 260 thousand points. The 3D target optimization takes between 3 minutes for a mesh of size  $321 \times 321$  to about 15 minutes for a  $641 \times 641$  mesh. All reported results are from a 2013 MacBook Pro with a 2.3GHz quad-core processor and 16GB of RAM.

The largest test case we ran took four hours of compute time to calculate the surface of a caustic generator of 1.5 million samples. More than 90% of the time is devoted to the optimal transport computation of which 99% of the time is spent recomputing the power diagram in each iteration. However, depending on the complexity of the target distribution, already significantly fewer samples suffice to achieve good results as listed in the table above.

**Ground truth comparison.** Figure 13 illustrates how our optimization approximates a ground truth result when increasing the resolution. For this example, uniform incident illumination on a circular domain is projected onto a uniform circular singularity curve centered at the origin. Through symmetry we see that under optimal transport each radial line is mapped to the corresponding closest point on the circle. For such a line, we can derive an analytic solution using Snell’s law that can then be radially swept to obtain the ground truth 3D shape of the generator. As the results indicate, our solution quickly approaches to the ground truth under refinement.

**Comparison to previous methods.** Figures 12 and 3 show a comparison of our approach to the methods of [Kiser et al. 2012] and [Yue et al. 2014], respectively. These methods achieve the highest quality caustic images to date. Both algorithms are similar in

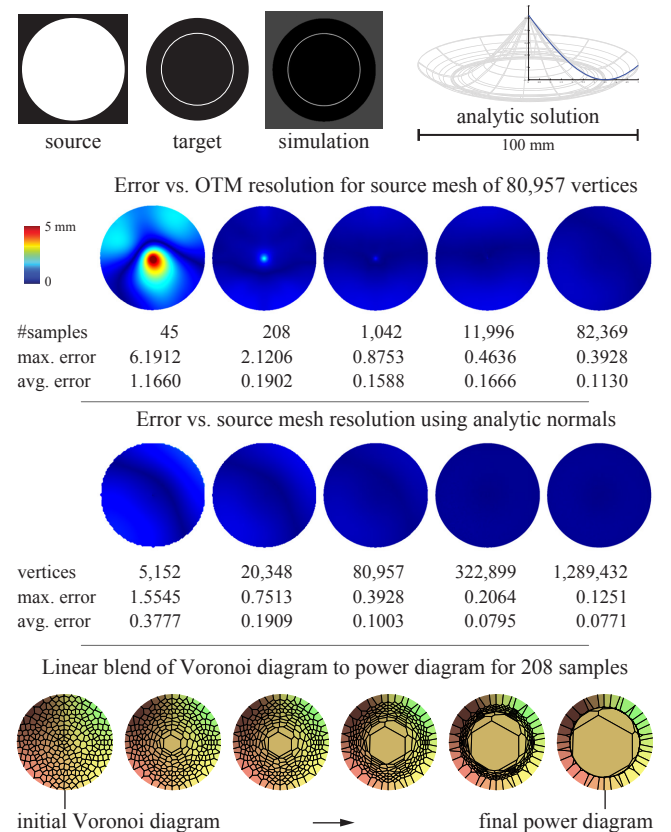


**Figure 13:** Ground truth evaluation. A disk of uniform light is focused onto a circular singularity curve by a hat shaped surface that can be computed in analytical form. All errors are in mm. The simulation shows the rendered caustic corresponding to an OTM resolution of 82,369 samples (top-right error plot).

that they use fixed boundary conditions and enforce smoothness of the generator surface everywhere. While suitable for low-contrast images, where both achieve excellent results (see Figure 14), these constraints lead to visible artifacts when aiming for high-contrast images or black regions. These artifacts can only be avoided by artificially reducing contrast. In Figures 3 and 12 this is achieved by increasing the brightness of the background to a point where a



**Figure 14:** For a smooth image like Lena, the performance of our algorithm is comparable to the state-of-the-art. For comparison, we use the input image as the basis for the gamma and global brightness of the other images. The top-right image has been provided by the authors of [Yue et al. 2014]. (Lena photo © Playboy Magazine)

substantial amount of light is “lost” for the actual caustic image. In contrast, our solution can harvest all light and supports completely black regions anywhere on the caustic. However, the adaptive discretization of the optimal transport algorithm comes at the price of increased computational overhead (see statistics above). The methods of [Kiser et al. 2012] and [Yue et al. 2014] that optimize on a regular grid are about 10 times faster, and therefore may still be preferable for low contrast images.

**Discussion and Limitations.** A key aspect of our algorithm is that optimal transport *automatically* determines where discontinuities in the normal field should occur. Instead of having discontinuities everywhere as in [Weyrich et al. 2009; Papas et al. 2011], or no discontinuities anywhere as in [Kiser et al. 2012; Yue et al. 2014], our approach strikes a balance that achieves superior image quality, while not imposing unnecessary restrictions on the achievable caustic images.

While our optimization supports singularities in the target distribution, physical models will always deviate from the perfect surface and blur out singularities to finite areas (see Figures 1 and 11). Explicitly modeling singularities is still useful, because it provides a more principled and complete mathematical formulation and avoids having to manually select the spatial width of high-intensity curves in a pixel grid. This could lead to excessive resolution of the input image and thus substantially increase computational cost.

The simplifying assumptions discussed in Section 2 incur a number of limitations of our approach. Area light sources, such as the sun, violate the assumption of a single incident light direction for each surface point. In general, this introduces blur in the caustic image, similar to the blur of shadow boundaries that cannot be avoided completely. Further blurring is introduced by imperfect specular scattering, machining imprecisions, and the necessary polishing

process to remove milling path artifacts. Despite the accumulative nature of these effects, our prototypes convey that physical realizations maintain the overall quality of the target caustic images. An interesting direction for future work, especially once machining precision improves, is to consider the wave nature of light and study the possible resolution of caustics at the limit imposed by diffraction and incorporate partial coherence as in [Levin et al. 2013].

Our optimization does not take into account potential self-shadowing, internal reflections, or physical limits of refraction. If the angle of the incident illumination on the source surface becomes too shallow, or the target normal deviates too strongly from the source normal, artifacts will occur.

Our approach solves for one specific mapping defined by the unique optimal transport map. While this mapping has several important benefits in terms of regularity and smoothness of the resulting caustic generator surface (see also the discussion in Section 4), potentially many other mappings exist for a specific target that might have interesting properties. For example, the optimal transport map by construction avoids fold-overs, which makes the caustic image rather stable under changes in the spatial configuration, e.g. when translating or rotating the piece with respect to the receiver (see also Figure 1). If a more fragile caustic image that exhibits more dynamic behavior is desired, mappings with fold-overs might be advantageous.

## 7 Conclusions

We have shown how an optimal transport formulation in combination with an iterative 3D optimization provides a powerful new tool for computational caustic design. Our method achieves comparable results to previous methods for low-contrast images, but yields significantly better results for high-contrast caustics. This is achieved by explicit modeling of singularities and automatic placement of discontinuities in the surface normals, made possible by an adaptive discretization that conforms to the target irradiance distribution. As a consequence, our algorithm significantly broadens the kind of caustic images that can be produced, attaining a new visual quality not possible before.

Our solution can serve as the basis for a number of future explorations. Extending the caustic design process to handle multiple source surfaces, consider the dynamics of caustics as the spatial configuration changes, or optimizing for multiple caustic images in a single object, are interesting questions for future research. More generally, our optimization algorithm is an example of performative form-finding: find a geometric shape that maximizes some performative goal, in our case the reproduction of a desired caustic image. This kind of optimization has many other potential applications, for example in geometry or image editing, digital fabrication, or physical simulation. The unique benefits of the optimal transport formulation can potentially be transferred to these domains, opening up numerous new research questions for computer graphics and related fields.

## Acknowledgements

We would like to thank Alfred Thomas, Nicolas Favre-Victoire and Claude Cheseaux from the EPFL ATPR workshop and Florian Rist of TU Vienna for the fabrication of the pieces. We thank Tuan Anh Le, Sofien Bouaziz for valuable discussion, and Yonghao Yue for providing images for comparison. We also thank the Philippe Halsman Archive for providing the Einstein photo. This research has received funding from the European Research Council under the European Union’s Seventh Framework Programme (FP/2007-2013) / ERC Grant Agreement n. 257453; COSYM.

## References

- AGARWAL, S., MIERLE, K., AND OTHERS. 2013. Ceres solver. <https://code.google.com/p/ceres-solver/>.
- AURENHAMMER, F., HOFFMANN, F., AND ARONOV, B. 1998. Minkowski-type theorems and least-squares clustering. *Algorithmica* 20, 1, 61–76.
- BOGACHEV, V. I. 2006. *Measure theory*. Springer.
- BOTSCH, M., KOBBELT, L., PAULY, M., ALLIEZ, P., AND LÉVY, B. 2010. *Polygon Mesh Processing*. Ak Peters Series. A K Peters.
- CHODOSH, O., JAIN, V., LINDSEY, M., PANCHEV, L., AND RUBINSTEIN, Y. A. 2013. On discontinuity of planar optimal transport maps. *arXiv/1312.2929*.
- DE GOES, F., BREEDEN, K., OSTROMOUKHOV, V., AND DESBRUN, M. 2012. Blue noise through optimal transport. *ACM Transactions on Graphics (TOG)* 31, 6, 171.
- DE PHILIPPIS, G., AND FIGALLI, A. 2013. The Monge-Ampère equation and its link to optimal transportation. *arXiv preprint arXiv:1310.6167*.
- FANG, F., ZHANG, X., WECKENMANN, A., ZHANG, G., AND EVANS, C. 2013. Manufacturing and measurement of freeform optics. *{CIRP} Annals - Manufacturing Technology* 62, 2.
- FINCKH, M., DAMMERTZ, H., AND LENSCHE, H. P. 2010. Geometry construction from caustic images. In *Computer Vision–ECCV 2010*. Springer, 464–477.
- GLIMM, T., AND OLICKER, V. 2003. Optical design of single reflector systems and the Monge-Kantorovich mass transfer problem. *Journal of Mathematical Sciences* 117, 3.
- HULLIN, M. B., IHRKE, I., HEIDRICH, W., WEYRICH, T., DAMBERG, G., AND FUCHS, M. 2013. Computational fabrication and display of material appearance. In *Eurographics State-of-the-Art Report*.
- KISER, T., AND PAULY, M. 2012. Caustic art. Tech. rep., EPFL.
- KISER, T., EIGENSATZ, M., NGUYEN, M. M., BOMPAS, P., AND PAULY, M. 2012. Architectural caustics - controlling light with geometry. In *Advances in Architectural Geometry*, Springer.
- LEVIN, A., GLASNER, D., XIONG, Y., DURAND, F., FREEMAN, W., MATUSIK, W., AND ZICKLER, T. 2013. Fabricating brdfs at high spatial resolution using wave optics. *ACM Transactions on Graphics (TOG)* 32, 4, 144.
- LIU, D. C., AND NOCEDAL, J. 1989. On the limited memory bfgs method for large scale optimization. *Mathematical programming* 45, 1-3, 503–528.
- MÉRIGOT, Q. 2011. A multiscale approach to optimal transport. In *Computer Graphics Forum*, vol. 30, Wiley Online Library, 1583–1592.
- PAPAS, M., JAROSZ, W., JAKOB, W., RUSINKIEWICZ, S., MATUSIK, W., AND WEYRICH, T. 2011. Goal-based caustics. *Computer Graphics Forum* 30, 2, 503–511.
- PATOW, G., AND PUEYO, X. 2005. A survey of inverse surface design from light transport behavior specification. In *Computer Graphics Forum*, vol. 24, Wiley Online Library, 773–789.
- PAULY, M., EIGENSATZ, M., BOMPAS, P., RIST, F., AND KRENMULLER, R. 2013. Controlling caustics. *Glass Performance Days*.
- SIBSON, R. 1981. A brief description of natural neighbour interpolation. *Interpreting multivariate data 21*.
- VILLANI, C. 2009. *Optimal transport: old and new*. Springer Verlag.
- WEYRICH, T., PEERS, P., MATUSIK, W., AND RUSINKIEWICZ, S. 2009. Fabricating microgeometry for custom surface reflectance. *ACM Transactions on Graphics (TOG)* 28, 3, 32.
- YUE, Y., IWASAKI, K., CHEN, B.-Y., DOBASHI, Y., AND NISHITA, T. 2012. Pixel art with refracted light by rearrangeable sticks. *Comp. Graph. Forum* 31, 2pt3 (May), 575–582.
- YUE, Y., IWASAKI, K., CHEN, B.-Y., DOBASHI, Y., AND NISHITA, T. 2014. Poisson-based continuous surface generation for goal-based caustics. *ACM Trans. Graph.* 33, 3 (May), 31:1–31:7.
- YVINEC, M. 2013. 2D triangulations. In *CGAL User and Reference Manual*, 4.3 ed. CGAL Editorial Board.
- ZHANG, Z., AND ZHENG, X. 2012. The representation of line Dirac delta function along a space curve. *arXiv preprint arXiv:1209.3221* (Sept.).